Creep behaviour at high temperature of a stabilized austenitic steel for Gen-IV nuclear power plants

L. Mateus Freire, E. Piozin, A. Courcelle, T. Guilbert, M. Sennour, . Gourgues a F

Creep behaviour at high temperature of a stabilized austenitic steel for Gen-IV nuclear power plants

Author(s) Name(s) and Affiliations(s)

L. Mateus Freire[1,2], E. Piozin[1], A. Courcelle[1], T. Guilbert[1], M. Sennour[2], A-F. Gourgues[2]

[1] DEN-Service d'Etudes des Matériaux Irradiés, CEA, Université Paris-Saclay, F-91191, Gif-sur-Yvette, France

[2] MINES ParisTech, PSL Research University, Centre des Matériaux, UMR CNRS 7633, BP87, 91003 Evry cedex, France

Contact data

(L.Mateus Freire, CEA and MINES ParisTech, lucie.mateus-freire@mines-paristech.fr)

Summary

ASTRID is a fast-reactor prototype for the 4th generation of nuclear power plants. The material used for fuel cladding is a cold-worked austenitic stainless steel called AIM1. This grade was developed to limit irradiation-induced swelling and improve microstructural stability and mechanical properties in normal operating conditions. In case of incidental situations, the cladding might rapidly reach higher temperatures (700-950°C) where its stability might be affected. The microstructural and mechanical behaviour in this temperature range is experimentally addressed in this paper.

Isothermal creep tests up to 1000°C under a wide range of stress levels enable to study viscoplastic flow, microstructural evolution under stress and damage/failure processes. In order to evaluate the effect of loading, microstructural characterizations (precipitation, recovery, and recrystallization states) on stress-free thermally-aged samples were also performed and compared with *post-mortem* examinations of creep specimens.

Up to 750°C, AIM1 shows better creep strength than previous generations of 15-15Ti grades. Beyond 750°C, dislocation mobility increases which promotes recovery and recrystallization processes. As a consequence, competition between work hardening due to viscoplastic deformation and softening due to dynamic recovery takes place. At 950°C, viscoplastic flow is strongly affected by recrystallization during creep test, especially in the tertiary stage. Softening due to gradual recrystallization leads to longer tertiary stages and higher ductility during tests under lower stress levels (about 40 MPa applied stress). Ductile fracture predominates at any temperature.

Characterizations on thin foils and carbon extractive replicas showed a large variety of precipitates, such as Cr-rich borides, phosphides, and Cr- and Ti-rich carbides.

Key Words

Austenitic stainless steel – creep – high temperature – recrystallization – recovery – precipitation

Introduction

ASTRID (Advanced Sodium Technological Reactor for Industrial Demonstration) is a fast-reactor prototype for the next generation of power plants in France. AIM1, which stands for Austenitic Improved Material #1, will constitute the first material for fuel cladding of ASTRID. This steel belongs to the 15%Cr-15%Ni, Ti-stabilized grade, and is used in a cold-worked (CW) state. The precipitation of nanometer-sized titanium carbides during high-temperature service (between 400 and 650°C) and the presence of titanium, silicon and phosphorus in solid solution is known to improve the resistance to radiation-induced swelling [1–5]. In addition, precipitation hardening in AIM1 improves mechanical properties at high temperature by pinning dislocations and delaying softening phenomena [6–8]. In the case of a hypothetical accident, the viscoplastic behaviour and the associated microstructural evolution beyond 650°C (precipitation, recovery, and recrystallization) are poorly known and have to be assessed. More generally, the viscoplastic behaviour of such a cold-worked, microstructurally unstable material is not clearly documented in open literature.

The aim of this work was to contribute to the understanding of microstructural evolution, deformation and rupture mechanisms of AIM1 under such unusual conditions, here, at 850°C and 950°C. Metallographic characterisations under stress-free thermal ageing and after creep tests at 850°C and 950°C were compared in order to dissociate the effects of mechanical loading on the microstructural evolution.

Experimental procedures

The chemical composition of AIM1 is presented in Table 1. This steel contains enough nickel and chromium to ensure a 100% austenitic matrix at room temperature as well as a high corrosion resistance. The amount of minor elements such as titanium, carbon, phosphorous, and boron have been optimized to improve the resistance to radiation-induced swelling and to creep at 650°C.

Element	Cr	Ni	Mo	Mn	Ti	Si	C	P	B
Minimum amount	14	14	1.3	1	0.3	0.7	0.08	0.03	0.004
Maximum amount	16	16	1.7	2	0.5	0.9	0.10	0.05	0.008

Table 1: specifications of the AIM1 chemical composition of (wt.%)

The material was investigated in the as-received condition. Final processing stages used to fabricate the AIM1 cladding tubes are illustrated in Figure 1. Solution annealing allowed homogenizing the microstructure by dissolving smaller strengthening precipitates. The final size and microstructure of the tube were obtained by cold drawing.

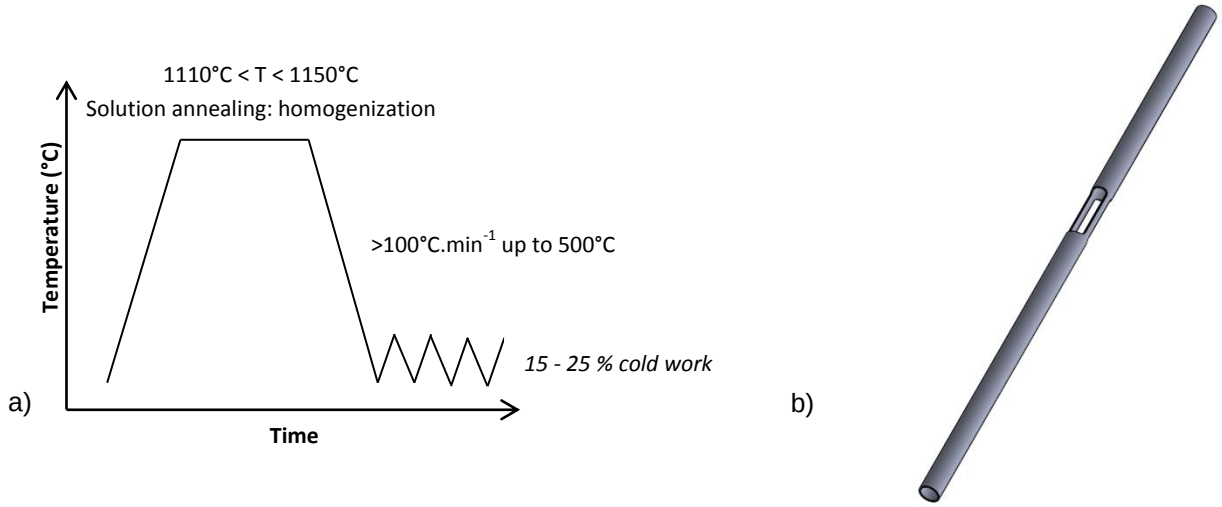

Figure 1: a) Final processing stages applied to the material under study and b) creep specimen geometry

Stress-free aging treatments were performed in a flowing helium quenching furnace (PYROX) at 850°C and 950°C up to 100 h. Sample were loaded in hot furnace and cooling by helium flowing. The heating rate was about 10°C.s^{-1} and the cooling rate between 1 and 10°C.s^{-1}. An high-speed dilatometer (DT1000) was used for aging treatments for times shorter than 2h for a tigher control of the temperature vs. time cycle (using the same heat rate as creep test furnace and a cooling rate from 100 to 200°C.s^{-1}).

Creep tests under uniaxial tension along the tube axis were performed under a secondary vacuum (10^{-4} mbar). The specimen geometry (gauge length 30 mm, total gauge section 3.4 mm²) is illustrated in Figure 1. The radiation furnace was controlled using a Pt/Pt-10%Rh thermocouple spot-welded to the specimen, close to the gauge region. Above 850°C, the thermal gradient across the gauge region was estimated to about 10°C from multiple thermocouple measurements. The heating rate was set to 5°C.s^{-1} up to 50°C below the test temperature, and then to 0.3°C.s^{-1} to the test temperature. The specimen temperature was stabilized for 5 min at 850°C, and for 1 min at 950°C before applying the constant load. Right after specimen fracture, the furnace was switched off in order to apply an average cooling rate of 3°C.s^{-1}. The elongation of the gauge part was continuously measured using high-temperature-resisting markers and monitoring the test with a 4Mpx digital camera equipped with special filters. The average elongation was then determined by digital image correlation.

The average hardness of as-received thermally aged and crept samples were determined from 42 indents using an applied load of 0.1 kg and a dwell time of 15 s. In order to characterize the microstructural evolution of the austenitic matrix, electron backscatter diffraction (EBSD) investigations were performed in the plane containing the tube axis and the circumferential direction. The samples were slightly ground using SiC papers, then polished using diamond pastes down to the 1 µm grade, followed by a colloidal silica finish. A field emission gun scanning electron microscope (SEM) was used, with a high voltage of 15 kV, a tilt angle of 70°, a step size of 0.3 µm to get typical EBSD map size of 400 x 400 µm. Grain orientation spread (GOS) maps were used to quantify the fraction of recrystallized grains. The GOS parameter represents an average misorientation level of grain. In the present work, the recrystallized grains are characterized by a GOS value below 1°. Kernel average misorientation (KAM) maps

were used to get a qualitative view of the local strains in the microstructure. The calculation was performed on the third neighbour with a tolerance of 15°. The KAM maps were compared to the GOS maps, to confirm the presence of recrystallized grains. Transmission Electron Microscopy (TEM) was performed on both thin foils and carbon extractive replicas. Fracture surfaces of the creep specimens were observed by SEM.

Microstructure of the as-received, cold-worked AIM1

A metallography of the as-received material is shown in Figure 2. Primary coarse precipitates had not been dissolved after the homogenization process. Titanium carbo-nitride precipitates were distinguished by their polygonal morphology and yellowish colour [9]. Titanium-molybdenum carbides precipitates are spherical or elongated and from complementary scanning electron micrographs, their size are at least 100 nm. Large annealing twins and thin deformation twins were observed, denoting a low stacking fault energy [10].

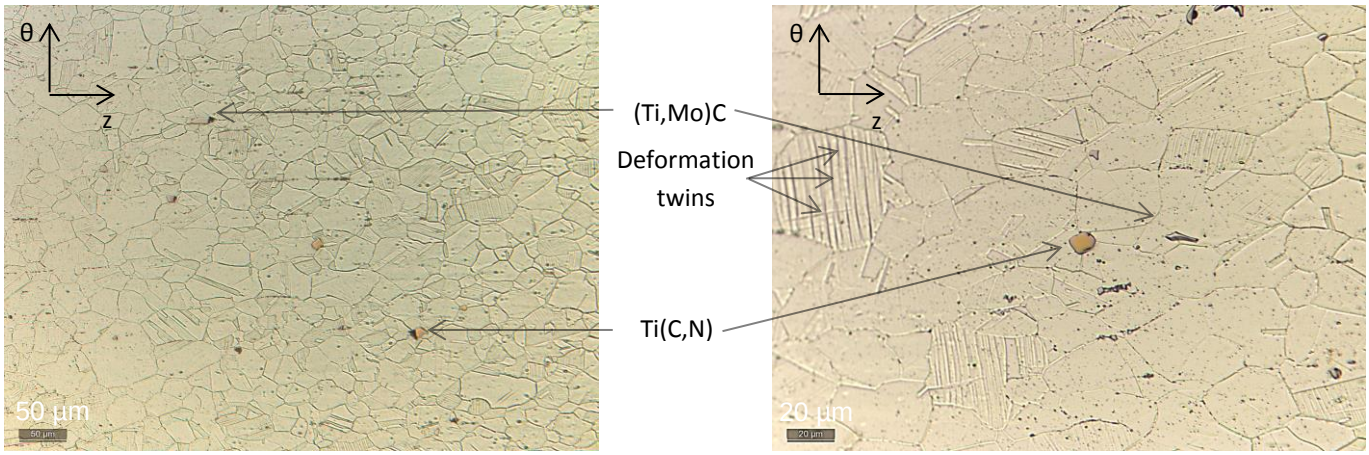

Figure 2: Optical micrographs after electrolytic etching showing large Ti(C,N) and primary (Ti,Mo)C and typical grain size of 30 µm..

TEM images of the initial microstructure are shown in Figure 3. Thin deformation twins and dislocation cells are visible in Figure 3. This microstructure is characteristic of a material with a high stored energy. As a consequence, exposure to high temperatures could lead to softening phenomena such as recovery or recrystallization [11].

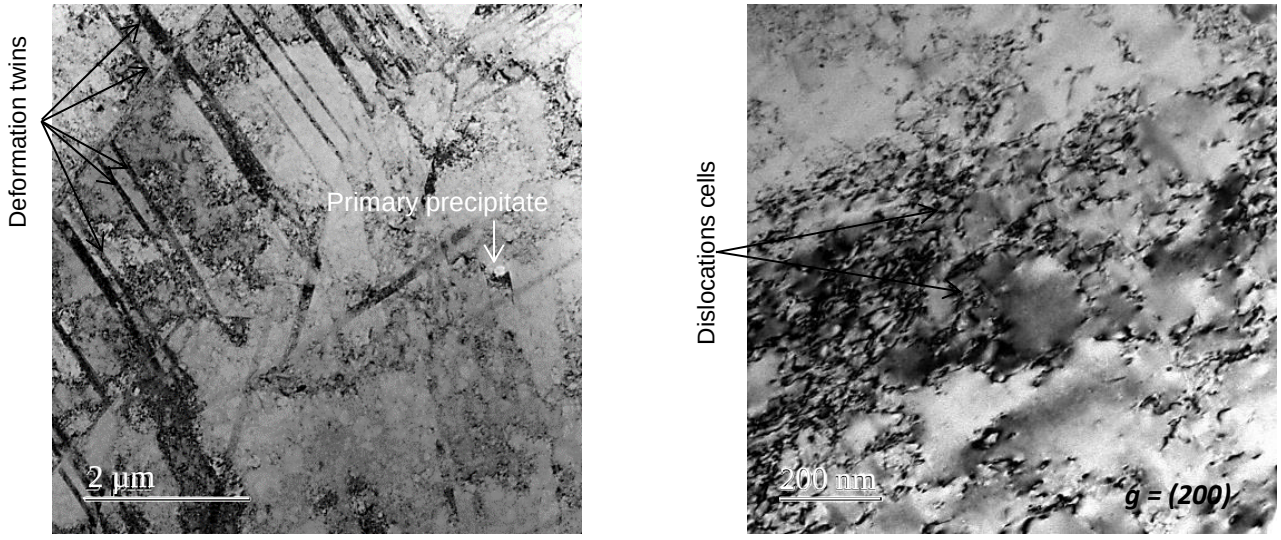

Figure 3: TEM bright-field images showing a) deformation twins and b) dislocation cells in the as-received material

Microstructural evolution under stress-free thermal ageing

Precipitation

After aging treatments, different types of precipitates were observed. With a phosphorus contents higher than 0.02 wt.%, phosphides can appear after aging in austenitic stainless steels [12-14]. As shown in Figure 4, needle-shaped phosphides were found after ageing at 850°C, but not at 950°C. Energy Dispersive Spectroscopy (EDS) showed that they were mainly Ti and Fe-rich.

Secondary titanium fine carbides, containing molybdenum are known to precipitate at dislocations below 650°C [6–8]. These precipitates were also found at 850°C and 950°C. Two populations of precipitate sizes are present for partially recrystallized states. In cold-worked grains, all titanium-carbide precipitates were less than 10 nm in diameter. From [6,8], during recrystallization, these secondary precipitates dissolve, then again form at the moving boundary between recrystallized and unrecrystallized grain and then remain in the recrystallized grain. The size of these new TiC precipitates was higher than 30 nm and they were found, as expected, in the recrystallized grains only. An example of such carbides in a deformed grain is shown in Figure 5 a). In the case of partially recrystallized microstructures, larger precipitates were in fact observed (Figure 5 b). These precipitates could be pinning a grain boundary.

Despite titanium stabilization, Cr-rich precipitates such as Mo-free $(Cr,Fe)_2B$ and Mo-containing $M_{23}C_6$ were also found and formally identified using electron diffraction together with chemical analysis. The molybdenum content was used to easily distinguish these two types of precipitates (Figure 6). They were mainly observed at grain boundaries and are known to improve the high-temperature strength by stabilising them [15,16].

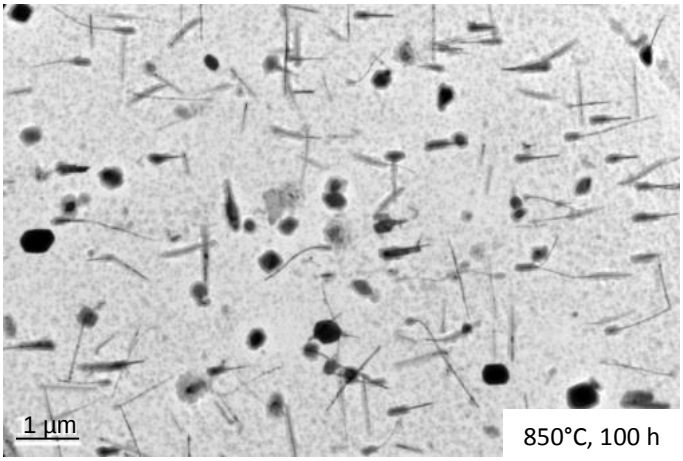

Figure 4 : TEM bright-field image showing round-shaped secondary (Ti,Mo)C and needle-shaped phosphorus-rich precipitates in a carbon extractive replica

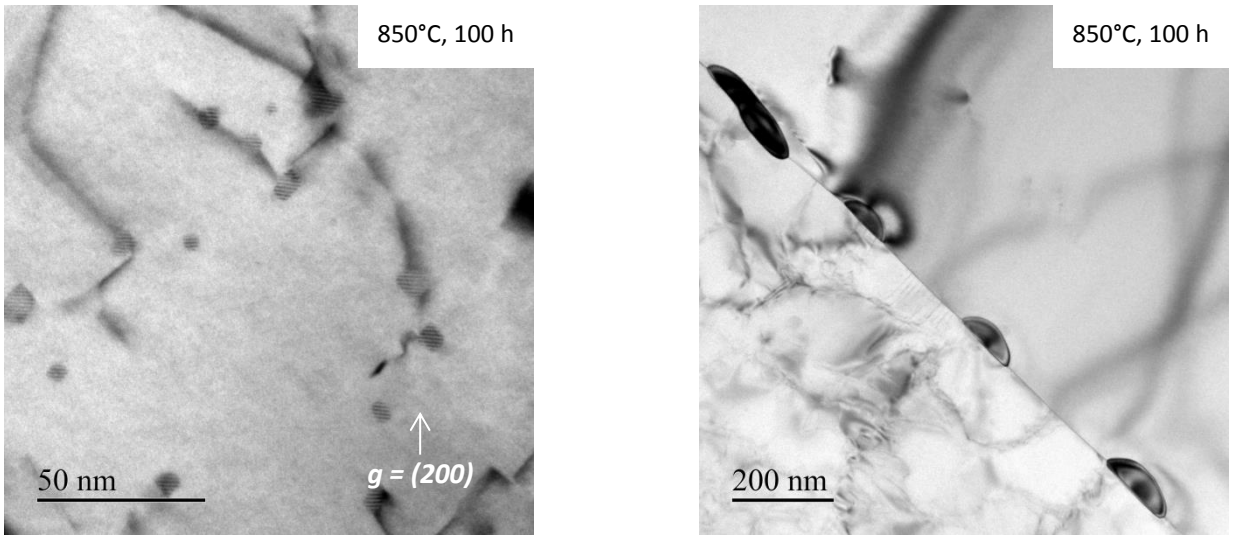

Figure 5: TEM bright-field image of thin foils showing a) secondary (Ti,Mo)C identified inside a cold-worked grain by using Moiré fringe contrast, and b) precipitates at a boundary between a cold-worked grain (left) and a recrystallized grain (right)

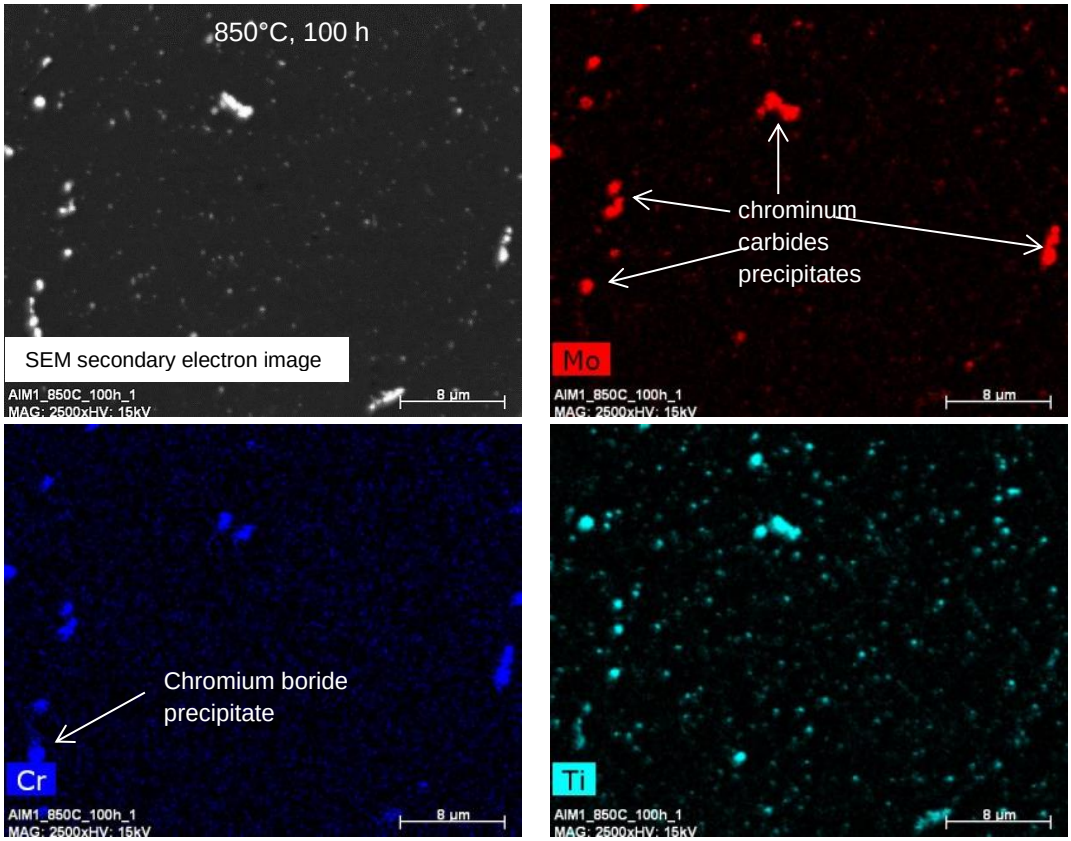

Figure 6: EDS elemental maps obtain by SEM on carbon replica showing Cr- rich particles after aging at 850°C, 100 h

Recovery and recrystallization

After aging, the average microhardness decreased although the experimental scatter remained high whatever the ageing conditions (Figure 7). The strengthening contribution due to precipitation was largely dominated by the loss of C and Ti in solid solution and/or by dislocation recovery and recrystallization. The recrystallized grain fraction obtained from GOS maps is illustrated in Figure 8 and plotted as a function of ageing time in Figure 7. The recrystallization kinetics was fairly well described by a Johnson-Mehl-Avrami-Kolmogorov (JMAK)-type equation [17, 18], yet with a temperature-dependent Avrami exponent (2.7 at 850°C and 1.0 at 950°C, respectively). From the comparison of recrystallized grain fractions and evolution of microhardness, softening at 850°C up to 24 h is probably a consequence of dislocation recovery. The drop in microhardness from 24 h at 850°C can be explained by the onset of recrystallization. At 950°C, the recovery kinetics is higher compared to 850°C and had already started after the first minute (0.017 h). The microhardness decreased more steadily at 950°C, even if recrystallization started after 0.5 h at triple junctions (Figure 8).

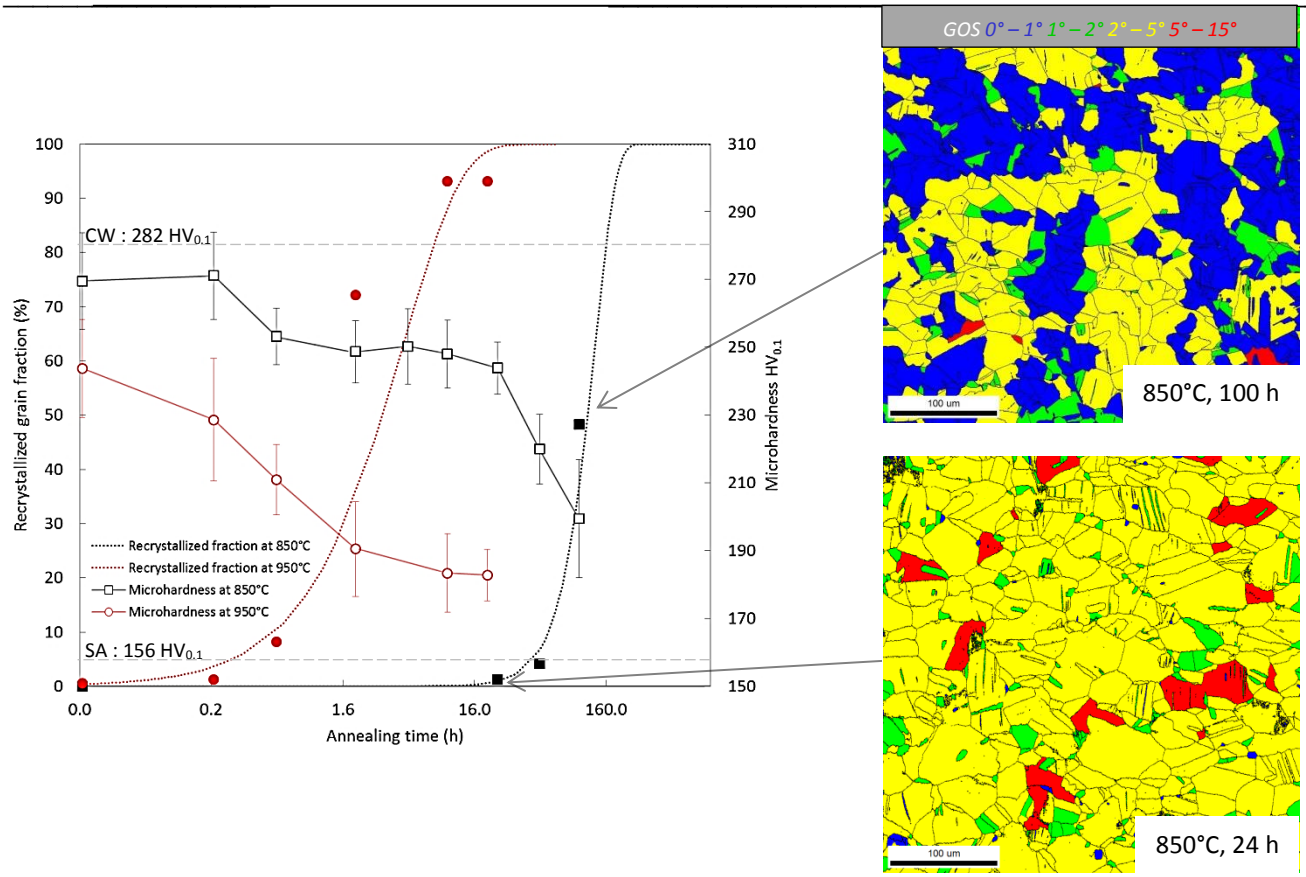

Figure 7: Microhardness evolution with time (open symbols) and recrystallization kinetics (full symbols: measurements; dotted lines: JMAK fit), stress-free aging at 850°C and 950°C

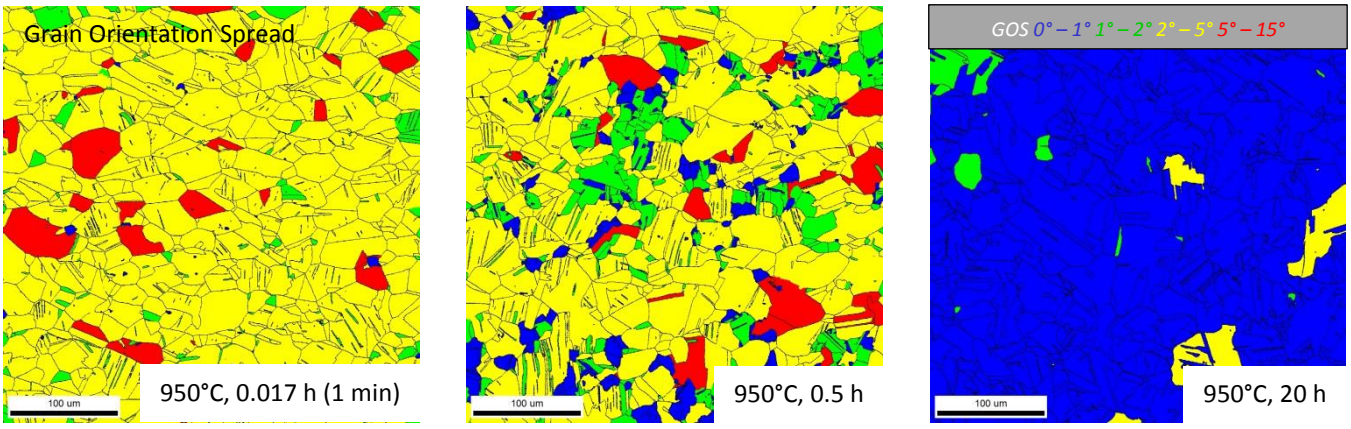

Figure 8: GOS maps showing microstructural evolution during aging treatments at 950°C

The growth of a recrystallized grain is illustrated in Figure 9. The difference in dislocation density dominated the retarding force due to curvature of the boundary between grain A and grain B, leading to growth of grain A at the expense of grain B. As in the example of Figure 9, precipitates can pin the recrystallization front.

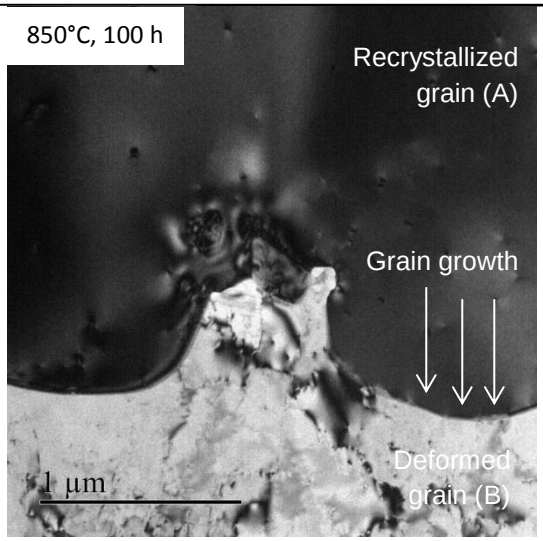

Figure 9: TEM bright-field image showing the recrystallization front pinned by precipitates

Creep flow and fracture behaviour and associated microstructural evolution

Viscoplastic flow at 950°C

Creep curves at 950°C under applied stress of 40 -100 MPa are presented in Figure 10 a). Figure 10 b) represents the thermal-mechanical cycle for creep tests that were directly performed on the CW state. The fracture elongation of AIM1 increases with decreasing the applied engineering stress. Under 40 MPa, the fracture elongation even reached 0.5. Moreover, the tertiary stage clearly represented the majority of the creep lifetime. From stress-free ageing at 950°C (see previous section), recrystallization occurs could be expected to begin after 30 min but the shape of the curves were not clearly correlated to the recrystallization kinetics. Recovery and recrystallization during creep tests imply competition between softening and strain hardening. In addition, titanium carbides precipitate preferentially at dislocations, and could contribute to the hardening during creep tests [19].

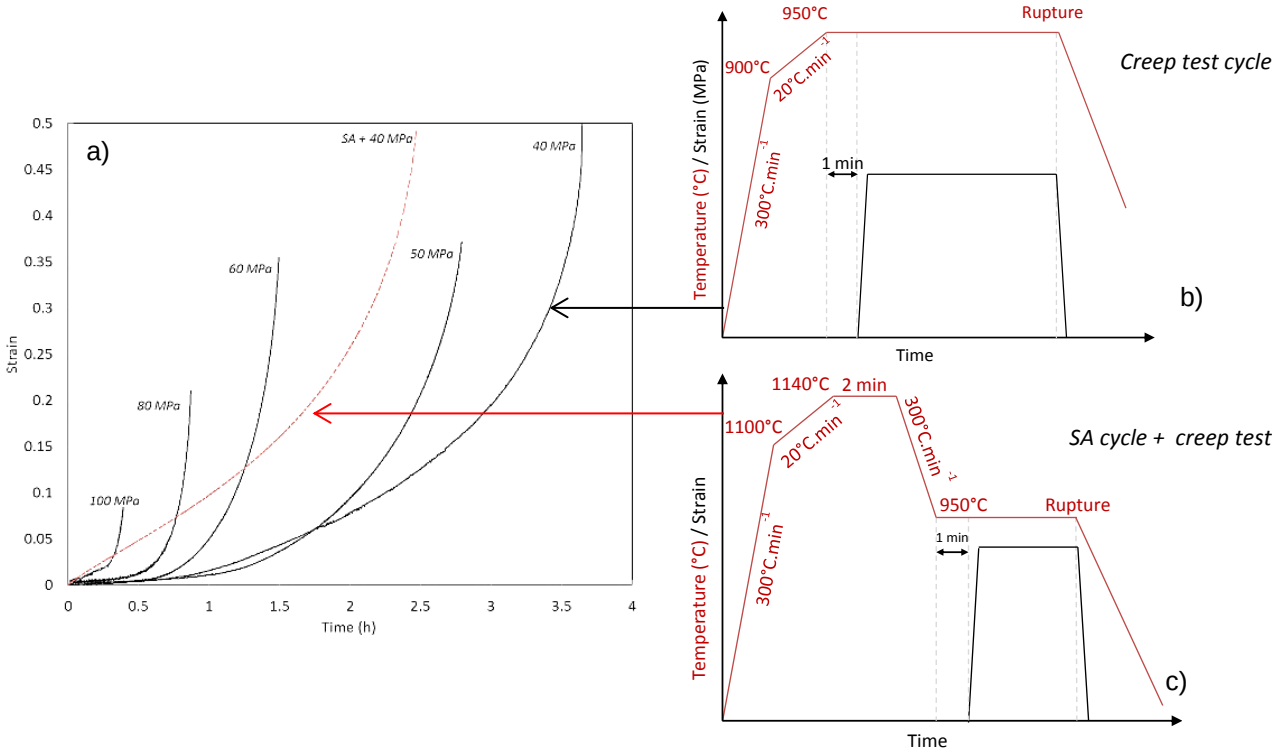

Figure 10 : a) creep curves at 950°C; thermal-mechanical cycles for creep tests b) on the CW state and c) on the in situ *SA state.*

In order to evidence the competition between strain hardening and recovery/recrystallization in a simpler starting microstructure, an additional test was performed on an *in-situ* solution-annealed (SA) specimen that was free from both residual strain and secondary precipitation (Figure 10 c). As-expected, the cold-worked material shows a better creep resistance to creep deformation than the solution annealed material from the very beginning of the test. This behaviour could be explained by either the much lower dislocation density or the absence of precipitation hardening at the beginning of creep. Moreover, the spatial distribution of precipitates formed during the creep test is probably different in the SA specimen and in the (initially) cold-worked specimens because of the difference in spatial dislocation distribution. Additional TEM observations are to be performed after interrupted tests to further address this point.

The minimum strain rates are plotted in Figure 11 as a function of engineering stress. Only one regime was found at 850°C; at 950°C, two regimes were tentatively distinguished, namely, a lower-stress regime with a rather low stress exponent, corresponding to creep of recrystallizing specimens, and a higher-stress regime corresponding to creep of a non-recrystallizing specimen, with a higher stress exponent, analogous to the case of 850°C. The calculated values of stress exponent, namely, between 2 and 7 are consistent with literature results reported for a stabilized austenitic stainless steel [20]. At 750°C, the reported value of about 9 [21, 22] was attributed to secondary carbide precipitation that increases the activation energy needed for creep deformation. At higher temperatures, precipitation hardening is less effective due to lower precipitate volume fraction and/or to easier dislocation cross-slip or climb, leading to lower stress exponents (about 4)[20].

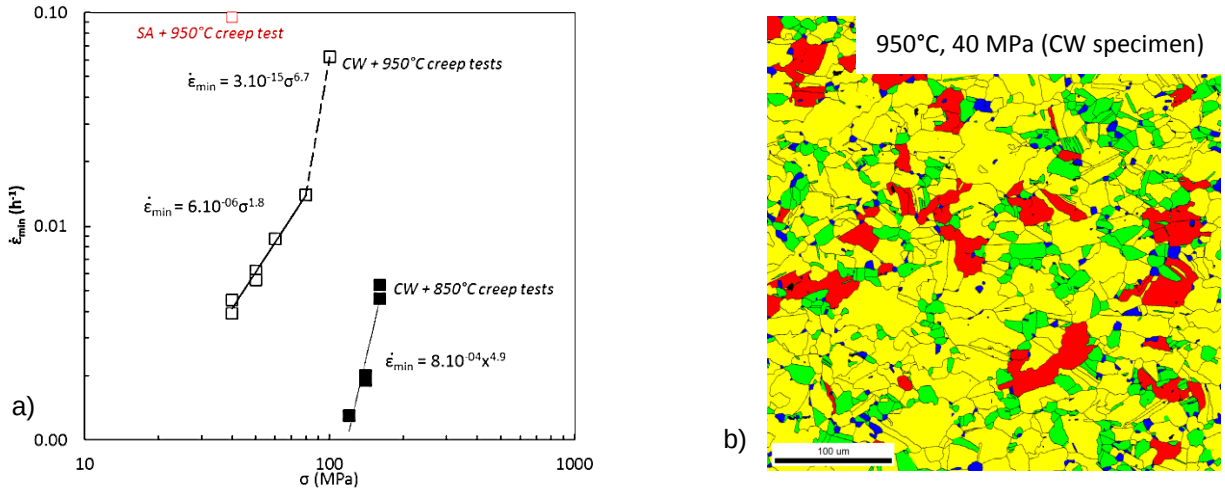

Figure 11 : a) Minimum creep rate vs. engineering stress curves from the creep results at 850°C and 950°C and b) GOS map of a creep test specimen

Fracture mode

For all creep tests, specimens failed by ductile fracture. At 950°C, fracture surfaces exhibited almost 100% reduction in thickness and some aligned dimples of about 1 µm in size (Figure 12), in agreement with the high fracture elongation. Inside dimples, polyhedral fragments were occasionally observed which suggested that damage initiated from large Ti (C,N) particles; this was confirmed by cross-section observations.

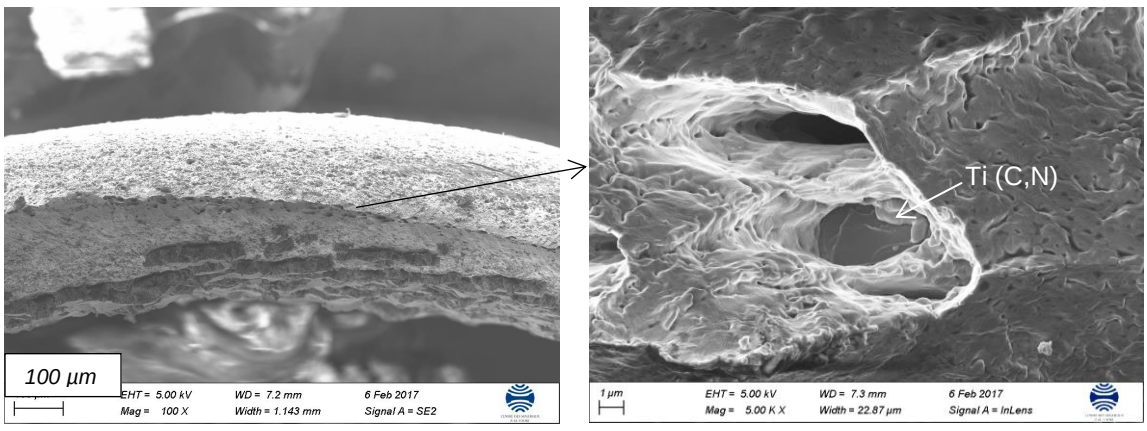

Figure 12 : SEM images of creep specimen fractured at 950°C under 40 MPa showing ductile fracture and large dimples.

Dynamic recrystallization

The microstructure of the SA specimen tested at 950°C is presented in Figure 13. Figure 13 a) confirms that the SA treatment followed by exposure at 950°C led to full recrystallization. Figure 13 b) shows the creep deformed microstructure of the same specimen. For the considered uniform elongation of 0.49, most of the grains were heavily deformed. However, nucleation of (blue) recrystallized grains, as well as the serrated shape of grain boundaries indicates that dynamic recrystallization mechanisms occurred during the creep test. Moreover, dislocation rearrangement into sub-grains was visible in the KAM map (Figure 13 c)). The comparison of these microstructures with those of initially cold worked specimens (Figures 8 and 9), shows that the initial microstructural state (dislocation density and/or amount of Ti and C in solid solution) greatly affects the microstructural evolution and corresponding creep strength at 950°C.

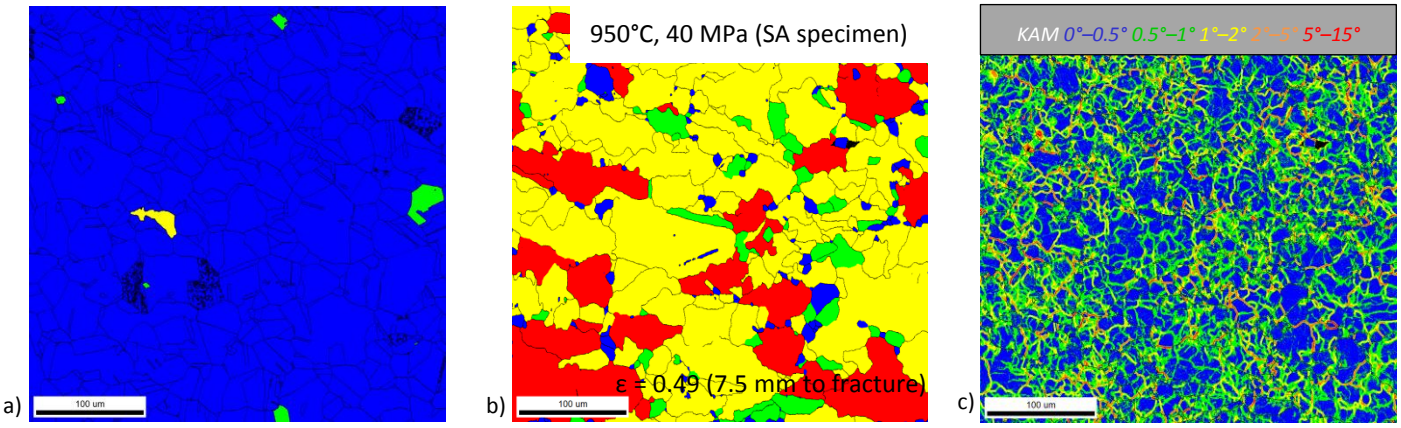

Figure 13 : a) GOS map of the undeformed part, b) GOS and c) KAM map of the same deformed gauge region of the SA specimen creep tested at 950°C under 40 MPa.

Conclusions

At 850°C, phosphides coexist with secondary Ti-rich carbides and Cr-rich precipitates. At 950°C and for partially recrystallized states, two populations of secondary Ti-rich carbides have been confirmed. Cr-rich precipitates were also observed, but no phosphide was found. Discontinuous recrystallization started by nucleation at grain boundaries after 24 h at 850°C and after 30 min at 950°C.

The viscoplastic behaviour of cold-worked material is dominated by tertiary creep and ductile fracture from primary nitrides, together with a high local reduction in thickness. The stress exponents are in agreement with literature findings in stabilised austenitic stainless steels.

In the solution-annealed specimen, the absence of fine precipitation and dislocation density at the beginning of mechanical testing limited the creep resistance by decreasing the minimum strain rate with respect to the cold-worked AIM1 material). In the SA state, a succession of dislocation hardening and recrystallization phenomena have occurred during the creep tests at 950°C, together with strong dynamic recovery and dynamic recrystallization. In contrast, despite the high amount of stored energy in the cold-worked microstructure, neither dislocation rearrangement nor serrated grain boundaries were observed after aging treatments.

Abbreviations

AIM1	Austenitic Improved Material #1
ASTRID	Advanced Sodium Technological Reactor for Industrial Demonstration
CW	Cold worked
EBSD	Electron Backscatter Diffraction
EDS	Energy Dispersive Spectroscopy
GOS	Grain Orientation Spread
JMAK	Johnson-Mehl-Avrami-Kolmogorov
KAM	Kernel Average Misorientation
SA	Solution annealed
SEM	Scanning Electron Microscopy
TEM	Transmission Electron Microscopy

Acknowledgments

The authors sincerely thank R. Clément (MINES ParisTech) for their technical assistance. Financial support from CEA and EDF are gratefully acknowledged.

References

[1] Lee, E. H.; Mansur, L.; Rowcliffe, A.: The effect of phosphorus on the swelling and precipitation behavior of austenitic stainless steels during irradiation; J. Nucl. Mater., 122 (1984), P. 299-304
[2] Watanabe, H.; Muroga, T.; Yoshida, N.: The temperature dependent role of phosphorus and titanium in microstructural evolution of Fe□Cr□Ni alloys irradiated in FFTF; J. Nucl. Mater., 228 (1996), P. 261-274
[3] Hamilton, M. L.; Johnson, G. D.; Puigh, R. J.; Garner, F. A.; Maziasz, P. J; Yang, W. J. S.; Abraham, N.: The effects of phosphorus and boron on the behavior of a titanium stabilized austenitic stainless steel developed for fast reactor service; ASTM Int., (1989)
[4] Seran, J. L.; Lévy, V.; Dubuisson, P.; Gilbon, D.; Maillard, A.; Fissolo, A.; Touron, H.; Cauvin, R.; Chalony, A.; Le Boulbin, E.: Behavior under neutron irradiation of the 15-15Ti and EM10 steels used as standard materials of the Phénix fuel subassembly; ASTM STP 1125, (1992), P. 1209
[5] Yvon, P.; Le Flem, M.; Cabet, C.; Seran J. L.: Structural materials for next generation nuclear systems: challenges and the path forward; Nucl. Eng. Des., 294 (2015), P. 161-169
[6] Kesternich, W.: Dislocation-controlled precipitation of TiC particles and their resistance to coarsening; 52 (1985), P. 533-548
[7] Kesternich, W.; Matta, M. K.; Rothaut, J.: Influence of TiC precipitation in austenitic stainless steel on strength, ductility and helium embrittlement; J. Nucl. Mater., 122 (1984), P. 130–133
[8] Kesternich, W.; Meertens, D.: Microstructural evolution of a Titanium-stabilized 15Cr-15Ni steel; Acta Metall., 34 (1986), P. 1071-1082
[9] Marshall P.: Austenitic Stainless Steels, Microstructure and Mechanical Properties; Elsevier Applied Science Publishers LTD, 1984.
[10] Padilha, A.; Plaut, R.; Rios P.: Annealing of cold-worked austenitic stainless steels; ISIJ Int., 43 (2003), P. 135–143
[11] Humphreys, F. J.; Hatherly M.: Recrystallization and Related Annealing Phenomena (Second Edition), Elsevier Ltd. 2004
[12] Lee, E. H.; Mansur, L. K.: Fe–15Ni–13Cr austenitic stainless steels for fission and fusion reactor applications. II. Effects of minor elements on precipitate phase stability during thermal aging; J. Nucl. Mater., vol. 278 (2000), P. 11-19
[13] Mandiang, Y.; Cizeron, G.: Phosphorus effects on microstructural evolution and phase stability in type 316 Ti stainless steels; Mater. Sci. Eng., 206 (1996), P. 233-240
[14] Mandiang, Y.; Azilinon, D.; Adj, M.; Cizeron, G.: Effect of phosphorus on stability of cold worked structure in 316Ti austenitic stainless steel; Mater. Sci. Technol., 16 (2000), P. 399-407
[15] Garcia-Borquez, A.; Kesternich, W.: TEM-studies on the borides formed in an austenitic steel with 38 ppm boron; Scr. Metall., 19 (1985), P. 57–62
[16] Schanz, G.; Padilha, A.: Precipitation of a boride phase in 15%Cr-15%Ni-Mo-Ti-B austenitic stainless steel (DIN 1.4970); J. Nucl. Mater., 95 (1980), P. 229-238
[17] Barraclough, D. R.; Sellars, C. M.: Static recrystallization and restoration after hot deformation of Type 304 stainless steel; Met. Sci., 13 (1979), P. 257-268
[18] Mandal, S.; Sivaprasad, P. V.; Dube, R. K.: Kinetics, mechanism and modelling of microstructural evolution during thermomechanical processing of a 15Cr–15Ni–2.2Mo–Ti modified austenitic stainless steel; J. Mater. Sci., 42 (2007), P. 2724-2734
[19] Kesternich, W.: Microstructural evolution and mechanical properties of an advanced high-temperature steel; J. Nucl. Mater., 155-157 (1988), P. 1025-1031
[20] Petersen, C.; Schanz, G.; Leistikow, S.: High-temperature behavior of CrNi-steel DIN material no. 1.4970 cladding material with respect to advanced pressurized water reactor safety considerations; 80 (1988), P. 161-172
[21] Latha, S.; Mathew, M. D.; Parameswaran, P.; Bhanu Sankara Rao, K.; Mannan, S. L.: Thermal creep properties of alloy D9 stainless steel and 316 stainless steel fuel clad tubes; Int. J. Press. Vessels Pip., 85 (2008), P. 866-870
[22] Latha, S.; Mathew, M. D.; Parameswaran, P.; Bhanu Sankara Rao, K.; Mannan, S. L.: Creep behaviour of 14Cr–15Ni–Ti stainless steel at 923K; Mater. Sci. Eng. A, 527 (2010), P. 5167-5174